MNRAS **000**, 1–11 (2020) Preprint 23 October 2020 Compiled using MNRAS LATEX style file v3.0

A broadband radio study of PSR J0250+5854: the slowest known pulsar

Crispin H. Agar,[1]★ Patrick Weltevrede,[1] and More Authors[2]
[1]*Jodrell Bank Centre for Astrophysics, School of Physics and Astronomy, University of Manchester, Manchester M13 9PL, UK*
[2]*Affiliations of other authors*

Accepted XXX. Received YYY; in original form ZZZ

ABSTRACT

We present simultaneous observations of the slowest-known radio pulsar PSR J0250+5854 with the Five-hundred-metre Aperture Spherical Telescope (FAST) and three LOFAR international stations Chilbolton, Effelsberg, and NenuFAR. The detections with FAST at 1250 MHz and NenuFAR at 57 MHz are the highest- and lowest-frequency detections respectively to date, and represent a five-fold increase in the spectral coverage of this object. We measure a flux density of 4 ± 2 μJy at 1250 MHz and an exceptionally steep spectral index of $-3.5^{+0.1}_{-0.5}$, with a turnover below ∼95 MHz. In conjunction with observations of this object with GBT and the LOFAR core, we show that the profile widths becomes broader with increasing frequency, contrary to the predictions of conventional radius-to-frequency mapping. Polarimetric data with FAST and the LOFAR core are used this to constrain the geometry of PSR J0250+5854. This leads to the conclusion that its radio emission height is similar to other rotation-powered pulsars, and much lower than for radio-detected magnetars.

Key words: pulsars: individual (PSR J0250+5854) – stars: neutron – polarisation – stars: magnetars

1 INTRODUCTION

Pulsars are rapidly-rotating, highly-magnetised neutron stars; however, some pulsars rotate significantly less quick than others. In this paper we discuss observations of PSR J0250+5854, a radio pulsar with a period $P = 23.5$ s discovered by Tan et al. (2018) in the Low Frequency Array (LOFAR) Tied-Array All-Sky Survey (Sanidas et al. 2019). It was detected with the LOFAR High Band Antenna array between 120-180 MHz, and with the Green Bank Telescope (GBT) at 350 MHz. It is the longest-period radio pulsar discovered to date, more than twice the period of the second slowest (PSR J2251−3711 at $P = 12.1$ s Morello et al. 2020) and almost three times slower than the well-studied 8.5-second pulsar PSR J2144−3933 (Young et al. 1999). Finding such a slow pulsar is rare, which can be explained by the fact that slower pulsars lose their ability to create electron-positron pairs, and accelerate them sufficiently to produce the detectable coherent radio emission (Sturrock 1971). In addition, there are practical issues with detecting slow pulsars because they are significantly harder to identify in pulsar survey data if only a small number of pulses are present. The presence of red noise in periodicity searches further hinders their identification (e.g. van Heerden et al. 2017).

Although the extreme period of PSR J0250+5854 would associate it with the magnetars which have periods of 2–12 s (Olausen & Kaspi 2014), its spin-down rate of $\dot{P} = 2.72 \times 10^{-14}$ s s^{-1} is low. As discussed in Tan et al. (2018), this means it lies in a relatively empty part of the P-$\dot{P}$-diagram, beyond the death line as defined by Chen & Ruderman (1993) and the vacuum-gap curvature radiation death line proposed by Zhang et al. (2000). It is also close to the area of the diagram inhabited by the population of X-ray Dim Isolated Neutron Stars (XDINSs). These objects are detected only as soft thermal X-ray sources without radio counterparts. Of the seven brightest XDINSs five have high magnetic dipole fields of the order 10^{13}–10^{14} G which may mean they are related to magnetars (Haberl 2007; van Kerkwijk & Kaplan 2007). However, to date PSR J0250+5854 remains undetected in X-rays, despite a dedicated *Swift* X-Ray Telescope observation (Tan et al. 2018). As of yet, PSR J0250+5854 has not shown any magnetar-like behaviour.

In this work we present the first detection of PSR J0250+5854 at a frequency of 1250 MHz using the Five-hundred-metre Aperture Spherical Telescope (FAST), along with simultaneous observations with the Chilbolton, Effelsberg, and NenuFAR LOFAR international stations. The NenuFAR detection at 57 MHz is the lowest frequency detection of PSR J0250+5854 to date, and the FAST detection the highest, resulting in an extension by a factor of ∼5 in spectral coverage of this unique source in the radio domain. The evolution of radio pulsar emission with frequency is a key part of understanding their emission mechanism, especially for such an unusual pulsar as PSR J0250+5854. Multi-wavelength observations can provide information on features including the spectral index (how the flux

★ E-mail: crispin.agar@manchester.ac.uk

of the pulsar changes with frequency), and changes in the shape and polarisation properties of the radio beam.

Measurements of pulsar radio spectra from a large population began with Sieber (1973), Malofeev & Malov (1980) and Izvekova et al. (1981) using frequencies around and below 100 MHz. Most pulsars were found to have steep spectra which could be modelled with a simple power law $S_\nu \propto \nu^k$, where S_ν is the mean flux density at some frequency ν and k is the spectral index. For some pulsars deviations from this relation were identified in the form of a turn-over at low frequencies which can be attributed to absorption mechanisms, whilst others show a cut-off at high frequencies due to a steepening or break in the spectrum (Sieber 1973). Recently, Jankowski et al. (2018) studied 441 pulsars and found that 79 per cent obeyed a simple power law relation. The distribution of spectral indices is described by a shifted log-normal distribution with a weighted mean of -1.60 ± 0.03 and a standard deviation of 0.54. Tan et al. (2018) were able to detect PSR J0250+5854 over a number of frequency bands between 120 and 350 MHz, and fitted a spectral index of -2.6 ± 0.5, which is steep but not unusually so. However, with a non-detection of the pulsar in Lovell (1484 MHz) and Nançay (1532 MHz) radio telescope data, nor a detection at 55 MHz with the core LOFAR Low Band Antenna stations, uncertainty remained over the broadband shape of the radio spectrum.

With its period of 23.5 s, PSR J0250+5854 has an extremely large light-cylinder (with a radius $R_{\rm LC} = cP/2\pi = 1.123 \times 10^6$ km, where c is the speed of light), and hence a tiny polar cap (with a diameter of ~60 m) which connects to the open field line region. This implies that for typical emission heights the radio beam, and hence the duty cycle of the radio pulse, can be expected to be very narrow. Indeed Tan et al. (2018) reported a pulse width of only $\sim 1^\circ$ at 129, 168, and 350 MHz. The shapes of pulse profiles are in general observed to be frequency-dependent. Often, the profile width decreases with increasing frequency which suggests that higher-frequency emission is produced lower in the magnetosphere. This correlation is known as radius-to-frequency mapping (RFM hereafter). RFM was first theorised by Ruderman & Sutherland (1975) who related the emission height to the local plasma frequency in the magnetosphere. The electron density, hence plasma frequency, are expected to fall with increasing altitude, thereby predicting that the radio beam shrinks with increasing frequency. A number of pulsars have been found to deviate from this relation (e.g. Thorsett 1991; Chen & Wang 2014; Pilia et al. 2016) – this suggests that not necessarily the same magnetic field lines are active at all frequencies (or emission heights), resulting in the appearance and disappearance of profile components with observing frequency (e.g. Cordes 1978; Mitra & Rankin 2002). This can obfuscate the geometrical interpretation of measured profile widths. Radio polarisation data can help in disentangling these effects, although degeneracies often remain (e.g. Keith et al. 2010).

The structure of this paper is as follows. In Section 2 the new observations are described, followed by a brief explanation of the radio-frequency interference (RFI) excision techniques used. The analysis of the data as described in Section 3 is divided into three parts: pulse profile evolution with frequency, polarisation properties, and the spectral shape of the pulsar flux. These results are then discussed in a broader context in Section 4, and our conclusions are summarised in Section 5

2 OBSERVATIONS

As part of a shared-risk proposal, PSR J0250+5854 was observed on the 22nd May 2019 with FAST. FAST is a Chinese mega-science facility owned by the National Astronomical Observatories, Chinese Academy of Sciences (Nan et al. 2011). With an effective aperture of 300 m in diameter, it is the world's largest single-dish radio telescope, and is located in a natural depression in Guizhou Province. The central beam of the high-performance 19-beam receiver operating between 1 and 1.5 GHz (Jiang et al. 2020) was used. Three LOFAR international stations: Chilbolton (United Kingdom), Effelsberg (Germany), and NenuFAR (France) provided overlapping observations. Chilbolton is home to the UK LOFAR station UK608, and the DE601 station located at Effelsberg is operated by the GLOW (German Long Wavelength) consortium. They each consist of two sub-arrays: the High Band Antenna (HBA; 110–240 MHz) and Low Band Antenna (LBA; 30–80 MHz) (van Leeuwen & Stappers 2010; Stappers et al. 2011). NenuFAR (New Extension in Nançay Upgrading loFAR) is a 96-tile antenna array operating between 10 and 85 MHz (Bondonneau et al. 2018). It is located alongside and extends the Nançay LOFAR station (FR606). Table 1 shows a summary of the overlapping observations conducted. The LOFAR international stations were observing over the full duration of the FAST observations, and in the case of NenuFAR significantly longer.

As well as observing PSR J0250+5854, FAST also performed a ~15-minute observation of PSR J0139+5814 to validate the set-up of the observing system, prior to the slow pulsar observation. A noise diode signal was injected into the FAST multibeam receiver to allow polarisation calibration. PSR J0250+5854 was observed for two consecutive hours, interspersed with noise diode observations. Finally, the BL Lacertae object J0303+472 (Véron-Cetty & Véron 2006) was observed for purposes of flux calibration – this source was chosen due to its proximity to PSR J0250+5854.

All data was folded and dedispersed with DSPSR (van Straten & Bailes 2011) using the ephemeris and dispersion measure (DM) reported in Tan et al. (2018) to form a pulse sequence, and flux and polarisation calibration was done using PSRCHIVE (Hotan et al. 2004). Further processing made use of PSRSALSA (Weltevrede 2016)[1].

2.1 Data cleaning techniques

PSR J0250+5854 is a weak pulsar. This, in combination with its extraordinarily long period makes the analysis susceptible to radio-frequency interference (RFI) which affects the baseline level during a rotation period. A somewhat different approach to mitigate the effects of RFI was taken for the different datasets, guided by the nature of the RFI.

In all datasets the worst-affected frequency channels were identified and excluded from further analysis. The FAST data was affected by stochastic baseline variations that persisted throughout the observation, with a timescale somewhat larger than the pulsar's duty cycle. These baseline variations were removed by subtracting sinusoids plus a constant offset fitted to the off-pulse region for each rotation of the star in each frequency and polarisation channel independently. This ensures that the mean intensity of the off-pulse region is zero. The sinusoids were harmonics of the pulse period,

[1] https://github.com/weltevrede/psrsalsa

Table 1. Observation properties of the simultaneous observations. There is a full overlap of the data for the period during which FAST was recording data for PSR J0250+5854 on the 22nd May 2019.

Observation	Centre freq. (MHz)	Bandwidth (MHz)	Freq. channels	Start time (UTC)	No. pulses	Length (hh:mm:ss)	Longitude bins
FAST	1250.00	500.0	4096	02:34:07	100	00:39:13	8192
FAST	1250.00	500.0	4096	03:31:23	153	01:00:01	8192
GLOW	158.55	71.4	488	01:56:19	417	02:43:34	1024
Chilbolton	149.71	95.2	1952	02:02:50	382	02:29:50	8192
NenuFAR	56.54	75.0	384	02:03:18	1528	09:59:21	2048

and were fitted up to the 23rd harmonic. These sinusoids have periods which significantly exceed the duty cycle of the pulsar, hence the shapes of the pulses were not affected by this process.

The character of the RFI in the GLOW and Chilbolton observations was very different, appearing as short, bright, impulsive spikes orders of magnitude brighter than the pulsar signal. An effective approach to mitigation was to iteratively clip the brightest samples for each rotation of the star and each frequency channel individually. The clipping is done conservatively to ensure that the pulsar signal is unaffected. With the worst RFI suppressed, the remaining RFI and baseline variations were dealt with in the same way as with the FAST data.

The NenuFAR data was recorded during the commissioning phase of the instrument with a coherent de-dispersion pipeline (LUPPI; Bondonneau et al. 2020) operating in single-pulse mode. The observations were folded with DSPSR and a polynomial of degree two was subtracted from each sub-integration to suppress the effect of band variations. The data from two frequency bands were appended after correcting for the appropriate delay[2]. The observation was cleaned using CoastGuard (Lazarus et al. 2016) and finally dealt with in the same way as with the FAST data.

3 ANALYSIS AND RESULTS

3.1 Profile morphology and width evolution

Figure 1 shows the integrated pulse profile of PSR J0250+5854 as observed by the four telescopes in order of descending frequency. We also include the profile observed by the GBT at 350 MHz, and the LOFAR core detection at 148 MHz (an observation from 28 October 2017). The profiles for the LOFAR international stations are obtained from the full-length observation rather than only the overlap period with the FAST observation to increase the signal-to-noise ratio. This is motivated by the fact that no evidence that the profile shapes were changing during these observations was found.

The profiles of the simultaneous observations in Fig. 1 were aligned by correcting for geometric delays associated with the difference in location of the telescopes (taking right ascension to be $02^{d}50^{m}17\overset{s}{.}78$ and the declination to be $+58°54'01\overset{''}{.}3$ as measured by Tan et al. (2018)). In addition, the dispersive delay associated with the propagation of the signal through the interstellar medium (ISM) was accounted for by taking a DM of 45.281 ± 0.003 cm^{-3}pc (Tan et al. 2018). The uncertainty on the DM translates to an uncertainty on the dispersion delay between the highest frequency (FAST; 1250 MHz) and lowest frequency (NenuFAR; 57 MHz) observations of 3.9 ms, or around one longitude bin at the highest resolution shown in Fig. 1 (for the FAST and Chilbolton data). The NenuFAR data obtained during commissioning phase could not be aligned in this way, hence the peak of the profile was aligned visually with the Chilbolton profile peak.

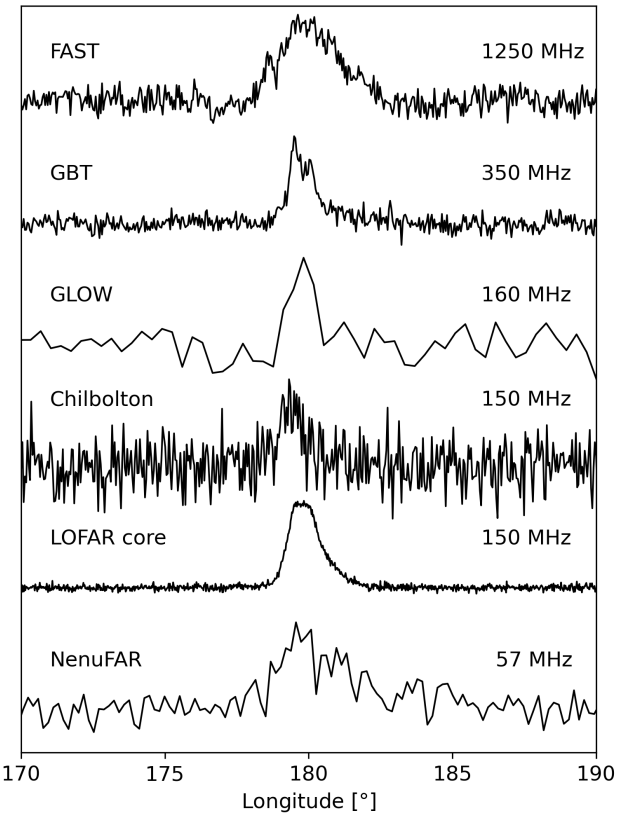

Figure 1. The pulse profiles of PSR J0250+5854 at different radio frequencies. The top profile is FAST (1250 MHz), followed by GBT (350 MHz), then GLOW (160 MHz), Chilbolton (150 MHz), LOFAR core (148 MHz), and finally NenuFAR (57 MHz). The FAST. GLOW, and Chilbolton profile data are overlapping in time, and are aligned using the known DM and after accounting for geometric delays. The NenuFAR profile data is also overlapping, but was visually aligned, as is the case for the other non-simultaneous observations.

Only the GBT profile has a clear double-peaked profile morphology. Although single-peaked, the LOFAR core profile, with a flat profile peak, and the asymmetric FAST profile can be taken as evidence for a more complicated profile structure. Looking at the profiles, it is evident that the profile width at frequencies below that of the FAST observation are significantly narrower, opposite to what is expected from RFM. The NenuFAR profile, corresponding to the

[2] This is only necessary for older observations conducted before the "early science" phase.

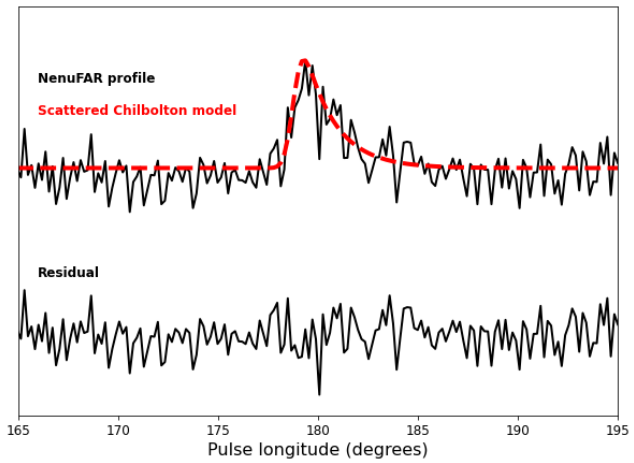

Figure 2. The NenuFAR profile (top) compared to a smoothed Chilbolton profile convolved with a scattering tail (dashed model curve, red in the online version). No significant signal remains in the residuals (bottom).

lowest frequency, is broader again and distinctly skewed. Given the steep rise followed by a tail, this can be attributed to scattering of the emission in the ISM. This is a strongly frequency-dependent effect with a power-law relationship between the scattering timescale and frequency, with a power law index of around −4 (Slee et al. 1980; Lyne & Graham-Smith 2012). This suggests that the scattering timescale for the NenuFAR data is around 50 times greater than at the Chilbolton centre frequency, which explains why only the NenuFAR profile is significantly affected. The NenuFAR profile is consistent with an intrinsic profile width which is equal to that observed at ∼150 MHz, albeit broadened by scattering. This is demonstrated in Fig. 2 where the NenuFAR profile is compared with a von Mises function with a width equal to that of the Chilbolton profile, and convolved with an exponential scattering tail with an e-fold timescale of 0.1 s. Therefore, scattering can fully explain the observed frequency evolution of the profile between 60 and 150 MHz. On the other hand, the high signal-to-noise (S/N) LOFAR core profile also shows an elongated tail, but this could not be attributed to scattering. No significant evolution of the profile was observed in the frequency-resolved data, with the tail being present across the band. It therefore appears that this feature is intrinsic to the profile. The S/N is too low in the Chilbolton profile for the tail to stand out. So we conclude that only the NenuFAR profile shows clear evidence for being scatter broadened.

To confirm and quantify the pulse broadening at higher frequencies, we measured the profile widths as shown in Fig. 1 by fitting von Mises functions to each profile. This smooth mathematical description of the profile allows the width to be measured without being strongly affected by (white) noise. Up to two components were required to model each profile, but including more than one component for low S/N profiles would result in over-fitting. The quoted uncertainties are calculated using bootstrapping where for each iteration a rotated version of the baseline was added to the profile. This ensures that both the statistical noise arising from the white noise as well as residual baseline variations are accounted for. The estimated full width at half maximum (W_{50}) of the profiles in order of increasing frequency are: 2.8 ± 0.4° (NenuFAR), 1.21 ± 0.03° (LOFAR core), 0.9 ± 0.1° (Chilbolton), 0.9 ± 0.1° (GLOW), 1.08 ± 0.07° (GBT) and 2.4 ± 0.1° (FAST). To further investigate the frequency evolution of the profile width, the widths were also determined after dividing the FAST data into four frequency sub-bands. Figure 3 shows the profile width against frequency for the profiles shown in Fig. 1 (black) and the FAST sub-bands (blue).

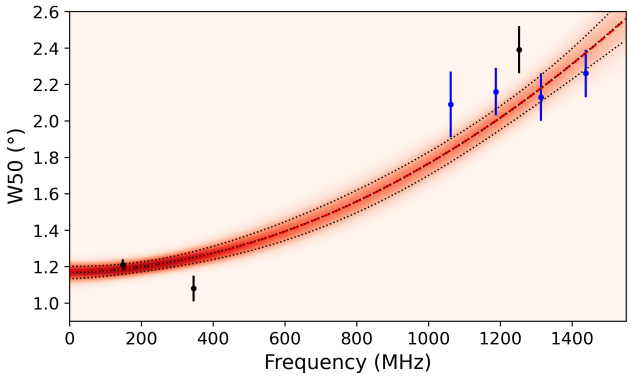

Figure 3. Evolution of the profile width of PSR J0250+5854 with observing frequency. Points in black correspond to the profiles shown in Fig. 1 and blue points are the profile widths of the four FAST sub-bands. The red line dashed represents the model of frequency evolution in Eq. (1) (Thorsett 1991) which was fitted to the FAST subbands, GBT, Chilbolton, and LOFAR core data (NenuFAR was excluded because it is affected by scattering). A distribution of fits was calculated using bootstrapping techniques, and is represented by the red colour gradient. The black dotted lines indicate the mean and $\pm 1\sigma$ contours of this distribution.

The evolution of profile width with frequency ν was modelled using the relation

$$W_{50} = A\nu^B + C, \quad (1)$$

where A, B, and C are constants (Thorsett 1991; Chen & Wang 2014). The fitting was done to the profile widths of the LOFAR core, Chilbolton, GBT, and FAST sub-band data. The NenuFAR profile was omitted to avoid scattering in the ISM affecting the results, and the GLOW and Chilbolton data were omitted because of their low S/N compared to the LOFAR core data at a similar frequency. The uncertainties on the fitted parameters were quantified by bootstrapping, and the distribution of trend lines is shown in the red gradient plot in Fig. 3. The black dotted lines represent the peak and 1σ contours of the distribution, as a function of frequency. The red dashed line represents the optimal fit to the data, and the power-law exponent of Eq. (1) is 1.9 ± 0.3. These findings will be discussed further in Sec. 4.

3.2 Polarisation and geometry

Polarisation calibration was performed on the FAST data using PSRCHIVE, making use of a pulsed noise diode signal injected into the 19-beam receiver[3]. The multibeam receiver maintains a fixed orientation with respect to the sky during the observation, so no parallactic angle corrections have been applied. The polarised pulse profile of PSR J0139+5814 (not shown, see also Sec. 2) matches the results of Gould & Lyne (1998) (available on the European Pulsar Network (EPN) database[4]) very well. The LOFAR core data was not polarisation-calibrated using the LOFAR station beam model, but rather tied-array addition which incorporates data from different

[3] In addition, a sign change of Stokes U and V was required.
[4] http://www.epta.eu.org/epndb/

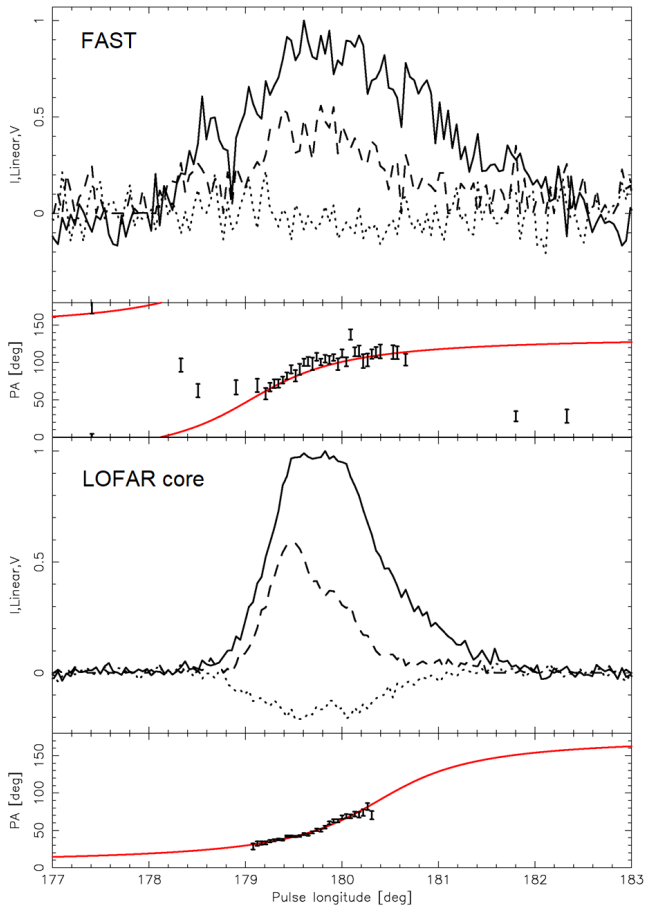

Figure 4. The polarised profile of PSR J0250+5854, observed with FAST (upper plot) and LOFAR (lower plot). Total intensity is shown as the solid line, linear polarisation as dashed and circular polarisation as dotted. The lower panel of each plot shows the variation of position angle of linear polarisation with pulse longitude. The Rotating Vector Model (red curve in the online version) was fitted to the LOFAR core data, and the same curve (with appropriate offset applied) is shown for the FAST data.

tiles and stations using the station calibration tables to account for the delays between them. As for the FAST data, the signs of Stokes V and the position angle curve had to be flipped in order to agree with IAU convention. A rotation measure RM = -54.65 ± 0.02 rad m^{-2} was fitted to the LOFAR core data, which is consistent with the Faraday rotation observed in the FAST data (although less well-defined at that frequency). Therefore the same RM was used to de-Faraday-rotate both observations.

In Figure 4 the polarised profile of PSR J0250+5854 is shown as observed with FAST (top panel), and the LOFAR core data (third panel). In both, the solid line is total intensity. The pulse profile has a moderate degree of linear polarisation (dashed), which was de-biased according to Wardle & Kronberg (1974). There is negative circular polarisation (dotted line) in the LOFAR observation, and a hint of the same in the FAST data.

The PA (ψ) as a function of pulse longitude is shown in the second and fourth panels, which relates to the Stokes parameters U and Q via $\psi = 0.5 \arctan(U/Q)$. Its functional shape can be explained by the Rotating Vector Model (RVM; Radhakrishnan & Cooke 1969), a geometric model which links the observed changes in PA with pulse longitude (ϕ) to the orientation of the magnetic

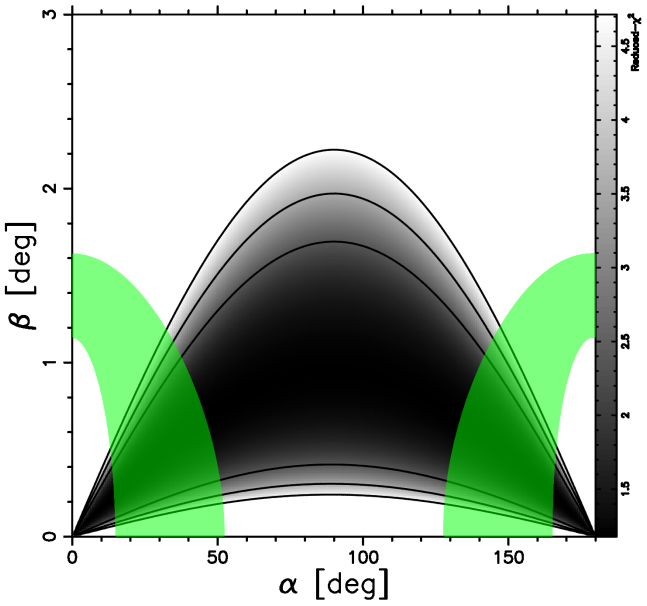

Figure 5. The goodness-of-fit (reduced chi-squared) of the Rotating Vector Model to the PA curve as a function of (α, β) space obtained for the LOFAR core data is shown in grey-scale. The black contours correspond to a reduced chi-square of 2, 3, and 4. The green transparent regions are the "allowed" viewing geometries, which are constraints arising from the estimated emission height and observed profile width (see the main text for details including the assumptions made).

field lines with respect to the observer and therefore depends on the inclination angle α of the magnetic axis, and the impact parameter of the observer's line of sight, β. It can be expressed as

$$\Delta\psi = \arctan\left(\frac{\sin(\Delta\phi)\sin\alpha}{\sin(\zeta)\cos\alpha - \cos(\zeta)\sin\alpha\cos(\Delta\phi)}\right), \quad (2)$$

where $\Delta\psi = \psi - \psi_0$, $\Delta\phi = \phi - \phi_0$, and $\zeta = \alpha + \beta$. It describes a monotonic S-shaped curve where (ϕ_0, ψ_0) is the location of the inflection point. The inflection point is where the gradient of the curve is steepest, with a gradient equal to $\sin\alpha/\sin\beta$ (Komesaroff 1970). The relatively steep gradient of the PA curve (~40 deg deg^{-1}) implies that $\beta \ll \alpha$, as expected for a slowly rotating pulsar with a narrow emission beam pointing in the direction of the magnetic axis.

To fit the RVM, a grid search (for details, see Rookyard et al. 2015) over pairs of α and β values for the LOFAR core observation was conducted. The best fit is shown in Fig. 4 for both the LOFAR and FAST data (after applying an offset in PA to account for the fact that no absolute PA calibration has been performed). The functional shapes of the LOFAR and FAST PA data are identical within the errors, as expected when a dipolar field line configuration determines the shape. We therefore will only consider the RVM fit to the higher S/N LOFAR core data.

The goodness-of-fit is parametrised by the reduced-χ^2 and its variation is shown in Fig. 5. The darker shading corresponds to lower reduced-χ^2 values and so a better fit. The black contours indicate 1σ, 2σ and 3σ confidence intervals. As can be expected for a pulsar with a very small duty-cycle, α and β are highly correlated. The fit confirms that β must be small ($< 2.2°$). However, the magnetic inclination α is unconstrained from RVM fitting alone.

The measured profile widths provide additional information about the opening angle of the radio beam, how the line of sight cuts

it, and the emission height. We assume that all radiation of a given frequency is produced at some height $h_{\rm em}$ in the magnetosphere in a circular region surrounding the magnetic axis. The emission beam is delimited by tangents to the last open field lines, forming a conal beam. In the small angle limit (e.g. $h_{\rm em} << R_{\rm LC}$, Rankin 1990) the half opening angle of the emission cone is

$$\rho = \sqrt{\frac{9\pi h_{\rm em}}{2Pc}}. \quad (3)$$

This implies that the radio beam widens with increasing emission height, and longer period pulsars can be expected to have narrower beams.

The width of the pulse profile depends on how the line of sight cuts through the emission beam, as determined by α and β. Gil et al. (1984) showed that the rotational phase range for which the line of sight samples the open-field-line-region, W, can be expressed as

$$\cos\rho = \cos\alpha\cos(\alpha+\beta) + \sin\alpha\sin(\alpha+\beta)\cos\left(\frac{W}{2}\right). \quad (4)$$

This means that a measurement of W can help to constrain the parameters α and β, as well as $h_{\rm em}$ via ρ (see for example Rookyard et al. 2015). Here it is important to note that the open-field-line region does not necessarily emit over its full extent, hence the measured profile width does not necessarily correspond to W as defined in Eq. (4).

Fig. 5 highlights the geometries which are compatible with the observed pulse widths of the FAST observation ($W_{10} = 4.4 \pm 0.2°$; the width of the profile as defined at 1- per cent of the peak flux density) shown as the green shaded region. Here it is assumed that the beam is fully illuminated and that the emission height lies within the range of 200 to 400 km (e.g. Mitra & Rankin 2002; Johnston & Karastergiou 2019). Moreover, W as defined in Eq. (4) is assumed to be between the measured W_{10} and twice this value to account for potential underfilling of the radio beam. The uncertainty on the measured W_{10}, the emission height, and the filling fraction results in a range of contours in (α, β) space defined by Eqs. (3) and (4). These contours (green region in the online version of Fig. 5) show that β is likely $\leq 1.2°$, and suggests that the pulsar is relatively aligned. The emission geometry of PSR J0250+5854 will be further discussed in Sec. 5. It will be concluded that although the underfilling of the beam could be somewhat more extreme compared to what is used to make Fig. 5, the result would only be a very modest extension of the allowed geometries towards slightly more aligned magnetic inclination angles.

3.3 Flux density spectrum

With a factor of ~5 in spectral coverage, an attempt was made to quantify the spectral shape of PSR J0250+5854. Flux calibration of the FAST data was possible by utilising the observation of the nearby BL Lacertae object J0303+472, which was used as a reference source (see Sec. 2). This source, also known by the identifier 4C 47.08 (Véron-Cetty & Véron 2006), has a known flux density of 1.8 Jy at a wavelength of 20 cm (approximately 1500 MHz, so close to the centre frequency of the FAST data) as listed in the VLA Calibrator List[5]. The NASA/IPAC Extragalactic Database (NED)[6] entry for this object contains a list of flux densities of this source at different frequencies from a variety of publications. This reveals a significant scatter in flux density measurements of observations at similar frequencies. Therefore, we assign an uncertainty of 50 per cent to the flux density which is consistent with other work on pulsar flux density measurements (e.g. Sieber 1973). The flux density calibration was performed using PSRCHIVE, resulting in a flux density of PSR J0250+5854 at 1250 MHz of 4 ± 2 μJy. The S/N of the profile is consistent with what is predicted for this flux density by the radiometer equation (e.g. Lorimer & Kramer 2005). This flux density is below the upper limits at a similar frequency based on non-detections with the Lovell and Nançay telescopes (Tan et al. 2018).

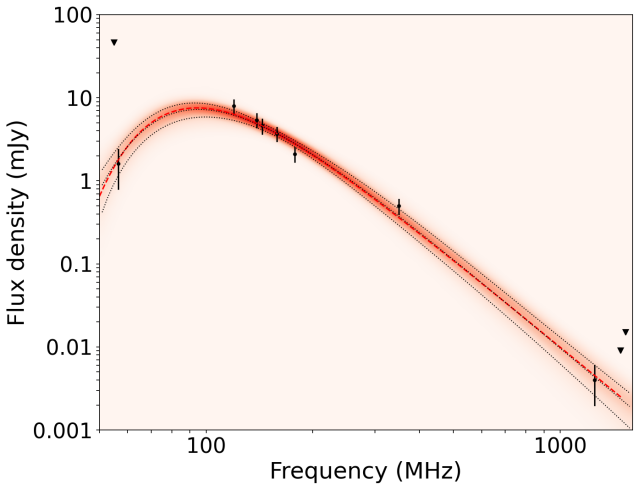

Figure 6. The flux density spectrum of PSR J0250+5854, including upper limits (inverted triangles) from previous non-detections (Tan et al. 2018). This plot includes the previous flux density measurements from Tan et al., with the new addition of the NenuFAR and FAST measurements. A power-law relationship with a low-frequency turnover was fitted to the data, and the best fit is indicated by the red dashed line. The distribution of acceptable fits is indicated, similar to Fig. 3.

Fig. 6 shows the flux density of PSR J0250+5854 as a function of observing frequency, and includes the flux densities previously measured by Tan et al. (2018). These previous measurements include detections with the GBT, LOFAR High Band Antenna array, and a flux density measurement obtained from a LOFAR Two-meter Sky Survey (Shimwell et al. 2017) image. PSR J0250+5854 was also detected with the NenuFAR array at 56 MHz, marking the lowest frequency detection. The flux density of the pulsar was estimated using the radiometer equation, and was found to be 1.6 ± 0.8 mJy, where we have again assigned a 50 per cent uncertainty. In calibrating this data the elevation of the source and number of antennae in the array were taken into account as they affect the gain, as was the band pass of the array. The sky background temperature was estimated to be 9050 K at the position of PSR J0250+5854, found by extrapolating the sky temperature measured at 408 MHz (Haslam et al. 1982) with a spectral index of −2.55 (Lawson et al. 1987; Reich & Reich 1988). This measurement indicates that the spectrum of PSR J0250+5854 rolls over at low frequencies, and this explains the upper limit at a similar frequency reported by Tan et al. (2018) based on LOFAR Low Band Antenna array observations. This spectral shape will be discussed further in Sec. (4.1).

[5] https://science.nrao.edu/facilities/vla/observing/callist
[6] https://ned.ipac.caltech.edu/

4 DISCUSSION

4.1 Flux density and spectral index

PSR J0250+5854 is weak at 56 MHz with the NenuFAR telescope, which is the result of a spectral turnover (see Sec. 3.3). This is not unusual in the pulsar population: for example, Jankowski et al. (2018) noted that 21 per cent of their sample deviates from a simple power law, exhibiting mainly broken power laws or low-frequency turnovers. The physical reasons for this are uncertain, but their analysis suggests that the deviations are partially intrinsic to the pulsar emission or because of magnetospheric absorption processes, and partially due to the environment around the pulsar. To quantify the spectral turnover, a power-law with a low-frequency turnover was fitted to the data using the same model used by (Jankowski et al. 2018), which is of the form

$$S_\nu = b\left(\frac{\nu}{\nu_0}\right)^k \exp\left(\frac{k}{m}\left(\frac{\nu}{\nu_c}\right)^{-m}\right), \quad (5)$$

where $\nu_0 = 500$ MHz is a constant (and arbitrary) reference frequency. The fitted parameters are b, a constant scaling factor; k, the spectral index; ν_c, the turnover frequency; and m which determines the smoothness of the transition. The value of m is expected to be positive, and ≤ 2.1.

With only one flux density measurement below the turnover frequency, the parameters are somewhat ill-defined. The optimal fit[7] (Fig. 6, red line) is for an exponent $m = 2.1$. This corresponds to the sharpest turnover allowed within the free-free absorption model (see Jankowski et al. (2018) and references therein). The fitted spectral index of $k = -3.5^{+0.1}_{-0.5}$ is steep compared to the mean found for the pulsar population (with a mean spectral index of -1.60 and a standard deviation of 0.54, Jankowski et al. 2018). But other examples of such steep spectral indices exist, including PSR J1234−6423 which has a broken power-law spectrum with a spectral index of -3.8 ± 0.5 below ∼1700 MHz (Jankowski et al. 2018).

Tan et al. (2018) noted that there are occasional bright pulses at 350 MHz (GBT data) in the leading component of the profile of PSR J0250+5854. This behaviour was not seen in the LOFAR observations at around 150 MHz. No bright single pulses were seen in the FAST data. However, given that the flux density of the pulsar is a factor of ∼100 lower at 1250 MHz this is not surprising. Reducing the S/N of the GBT data to make it comparable to that of the FAST data rendered the variability undetectable.

4.2 Profile width evolution

As can be seen in Fig. 3, the profile width of PSR J0250+5854 increases with observing frequency, from around 1° at 150 MHz to 2° at 1250 MHz. Eq. (1) was fitted to the measured profile widths as a function of frequency, resulting in a power-law index $B = 1.9 \pm 0.3$ (see Sec. 3.1). Although it is unusual for pulsars to have a positive index, meaning that their profiles broaden with increasing frequency, there are other examples. Chen & Wang (2014) identified 29 pulsars out of 150 with such a positive index based on profiles from the EPN database.Of those, none have a value of B which is significantly larger than that of PSR J0250+5854 given the relatively large uncertainty on both our measured value of B and those measured by Chen & Wang (2014). The index for PSR J0250+5854 is consistent with 24 out of the 29 pulsars with a reported positive index. This increase in profile width with frequency is counter to the expectation from RFM, and possible reasons will be discussed here.

Since one expects both the plasma density and the plasma frequency to decrease with altitude (e.g. Hibschman & Arons (2001) and references therein; also Gedalin et al. (2002)), higher frequency radiation can be expected to be produced closer to the neutron star if they are the result of plasma instabilities. Alternatively, if the radio emission is produced by curvature radiation from relativistic bunches of particles travelling along the magnetic field lines, he characteristic frequency of the radiation produced will also be higher near the surface of the neutron star given the smaller radius of curvature of the field lines (e.g. Gil et al. 2004; Dyks & Rudak 2015 and references therein). As a consequence the opening angle of the radio beam can be expected to be narrower at higher frequencies produced lower in the magnetosphere. However, exceptions can be expected if profile components appear or disappear at different observing frequencies, indicative of the fraction of the open-field-line region which is active to be frequency dependent. For example, Pilia et al. (2016) studied 100 pulsars and measured their profile widths at frequencies ranging from tens of megahertz up to 1400 MHz. They found that for the majority of cases, pulsars showed conventional-RFM characteristics, and sometime little frequency evolution of the pulse width at all. In a few cases (e.g. PSRs B1541+09, B1821+05, B1822−09, and B2224+65), the profile width was seen to increase with frequency. In these examples, profile broadening was indeed caused by the emergence of new profile components as frequency increased.

Given that the profile evolution of PSR J0250+5854 is asymmetric as a function of frequency (Fig. 1), this is suggestive of an emerging profile component at the trailing side of the profile at higher frequency, rather than being caused by a single widening component. Observations at a frequency around 800 MHz could reveal the reasons for the abnormal frequency evolution of the profile. The profile morphology of PSR J0250+5854 is indeed complex, with a profile shape skewed in both the LOFAR core and FAST observations. The GBT profile shows a distinct double-peaked structure with distinct behaviours since Tan et al. (2018) noted that the stronger first component was caused by occasional strong individual pulses. At other frequencies no well separated profile components are observed. However, the flattened peak in the LOFAR core profile is suggestive of two blended components of similar intensity. This flattening was not visible for the profiles published in Tan et al. (2018), which is because of the lower S/N. By inspecting all available data, no significant profile shape variability has been detected in LOFAR core observations of PSR J0250+5854.

Chen & Wang (2014) conclude that in a number of cases (PSRs B1818−04, B1851−14, B1900+01, B1915+13, B2053+36, and B2217+47) the widening of the profile at higher frequencies could not be ascribed to structures consistent with the core-cone model (e.g. Rankin 1983a,b; Radhakrishnan & Rankin 1990; Rankin 1993). This also appears to be the case in a small subgroup of pulsars studied by Pilia et al. (2016) (PSRs B0355+54, B0450+55, B1831−04, and B1857−26). Like PSR J0250+5854, these pulsars do not show well-separated profile peaks at the highest frequencies. This led Chen & Wang (2014) to suggest that fan beams could accommodate anti-RFM-like behaviour. The expectation from conventional RFM is based on emission being produced over a wide range of altitudes, and each height producing narrowband emission. On the other hand, if a narrow range of emission heights generates broadband emission the observed spectrum will

[7] The resulting probability density function of m is highly clustered at the maximum allowed value of 2.1 which was implemented as a prior. Therefore no meaningful uncertainty on m could be assigned.

be different. Broadband emission is incorporated into the fan beam model (Michel 1987; Dyks et al. 2010; Dyks & Rudak 2012, 2013; Wang et al. 2014) where emission is produced along magnetic flux tubes that extend out from the pole in a fan-like structure. Support for this beam structure is found in observations of the precessing pulsars PSR J1141−6545 and PSR J1906+0746 (Manchester et al. 2010; Desvignes et al. 2013). Following Michel's suggestion that each flux tube may have its own spectrum, Chen et al. (2007) argued that the emission spectrum may not be homogeneous across a flux tube. In particular, they argue that pulsars which show pulse broadening with increasing frequency may have a flattening emission spectrum away from the magnetic axis, as supported by their simulations. Broadband emission in flux tubes with a location-varying spectral index follows naturally from particle-in-cell simulations of vacuum-gap pair-production (Timokhin 2010) which predict that the momentum spectrum of the secondary plasma is not necessarily monotonic as a function of height within the magnetosphere and so a given observed frequency cannot be assigned to a unique altitude.

4.3 Emission height and viewing geometry

Constraining the viewing geometry is particularly interesting for slowly rotating pulsars to highlight differences with magnetars (see Sec. 4.4). As discussed in Sec. 3.2, RVM fitting to the PA swing confirmed that the radio beam of PSR J0250+5854 is very narrow by showing that the line-of-sight impact parameter $\beta \leq 2.2°$. However, the magnetic inclination angle α remained indeterminate.

Further constraints on α can be derived using knowledge of the emission height. As seen in Fig. 4, the inflection point of the PA swing occurs very close to the centre of the profile at both frequencies. This implies that the emission height must be considerably smaller than the light cylinder radius. If this were not the case, relativistic aberration and retardation (A/R) effects would shift the inflection point outside the duration of the pulse profile. Blaskiewicz et al. (1991) showed that the expected delay in pulse longitude between the inflection point and the longitude in the profile corresponding to the fiducial plane (the plane containing the magnetic and rotation axes) is $\Delta\phi = 4R_{\rm LC}/h_{\rm em}$. For example, for a fractional emission height $h_{\rm em}/R_{\rm LC}$ of 1 per cent (1.1×10^4 km) this equates to an offset of ∼2.3°. For PSR J0250+5854 this would mean that the inflection point of the PA curve should lie on the far trailing edge of the total intensity profile. The total intensity profile is asymmetric, making it difficult to accurately identify the position of the fiducial plane. Nevertheless, it is clear that the delay is small, implying an emission height considerably smaller than 1 per cent of $R_{\rm LC}$.

This conclusion confirms that radio pulsars produce emission at an absolute emission altitude that is relatively constant across the population, rather than being at a constant fraction of $R_{\rm LC}$. Indeed extending the empirical model of RFM for non-recycled pulsars by Kijak & Gil (2003) to the extremely long period of PSR J0250+5854 suggests emission heights of several thousand kilometres – from $1.2\pm0.3\times10^3$ km at FAST frequencies to $3\pm1\times10^3$ km at NenuFAR frequencies – consistent with the upper limit from our polarisation observations. Given the emission height is not at a constant fraction of $R_{\rm LC}$ there should be a period dependence of the pulse width (e.g. Rankin 1993). Based on this relationship Karastergiou & Johnston (2007) proposed that the maximum emission height of radio pulsars is around 1000 km, refined to an absolute height range of 200 to 400 km irrespective of pulse period (Johnston & Karastergiou 2019; Johnston et al. 2020). Again this is consistent with our results.

The profiles seen in Fig. 4 are aligned based on an ephemeris of the pulsar spin evolution. Given the small (fractional) emission height at all frequencies, the inflection points of the PA curves are expected to align, which they do within uncertainties. This further reinforces the validity of the alignment of the profiles in Fig. 1, and thereby the conclusion that the filling factor of the beam is frequency dependent, and so is the cause of the profile broadening at higher frequencies. The filling factor impacts the "allowed" viewing geometries highlighted in the green shaded region of the online version of Fig. 5. In Sect. 3.2 we assumed that the FAST profile occupies at least half the open field line region. This is based on the location of the PA curve inflection point, which is slightly earlier than the peak and midpoint of the profile (albeit with a degree of uncertainty).The span of W (eq. 4) used to make Fig. 5 represent two extremes: that the beam is either fully filled (within the uncertainties the PA inflection point lies at the midpoint of the profile), or is only half filled (the PA inflection point is also consistent with occurring at the leading edge of the profile). Further to these considerations, it cannot be ruled out that the trailing edge of the profile does not reach the edge of the open field line region. This would would correspond to a lower filling factor. However, even if the filling factor is decreased by a further factor of two, the minimum allowed α goes only from ∼15° to ∼10°. So even a large uncertainty in the actual filling fraction has a marginal effect on Fig. 5.

4.4 Comparison to other slow pulsars and magnetars

Radio magnetars are slowly rotating, hence comparing the radio-detected magnetars with PSR J0250+5854 and other extremely slowly rotating rotation-powered pulsars reveals differences which are not just the result of the slow rotation of these objects. Aside from PSR J0250+5854, the two other slowest known radio pulsars are PSRs J2251−3711 (P = 12.1 s), and J2144−3933 (P = 8.5 s). There are five known magnetars for which pulsed radio emission has been detected: 1E 1547.0−5408 (Camilo et al. 2007c), PSR J1622−4950 (Levin et al. 2010), PSR J1745−2900 (Eatough et al. 2013), XTE 1810−197 (Camilo et al. 2006), and Swift J1818−1607 (Esposito et al. 2020; Lower et al. 2020). A summary of their properties is shown in Table 2

A difference between magnetars and slow pulsars is that magnetars can have exceptional shallow radio spectra. PSR J1622−4950 has a flat spectrum between 1.4 and 24 GHz (Keith et al. 2011) similar to the spectra of 1547.0−5408 and XTE J1810−197 (Camilo et al. 2007c,a). In contrast, the spectral index of the slow pulsar PSR J0250+5854 is exceptionally steep ($-3.5^{+0.1}_{-0.5}$ compared to the a mean of −1.6 for the non-recycled pulsar population). However, the spectral index of the magnetar Swift J1818.0−1607 is relatively steep as well at $-2.26^{+0.02}_{-0.03}$ (Lower et al. 2020), which led them to believe there may be a link with the rotationally-powered PSR J1119−6127 (e.g Majid et al. 2017; Dai et al. 2018).

The three slow radio pulsars have long periods and narrow, fairly simple pulse profiles. Measurements of W_{50} are published for these profiles and are representative of the overall profile width. Despite being the slowest of the three, PSR J0250+5854 has the widest profile by around a factor of two. If only the period determines the width, the inverse would be expected. This suggests that besides PSR J0250+5854 (see Sec. 4.3) underfilling of the beam also plays a role in the other slow pulsars. In contrast, the magnetars have fairly complex profiles with multiple components of differing intensity, which means that W_{50} is not always a representative number for the overall width of the profile. Therefore, for the magnetars the profile width as quoted in Table 2 spans the region where the emission

Table 2. Parameters (period P, spin-down rate $\dot{P}$) of the three slowest radio pulsars (top three sources) and the five magnetars (lower five sources) known to produce pulsed radio emission. The profile width of the radio pulsars are measured values of W_{50} taken from this work and the referenced literature. The widths of the magnetar profiles are estimated based on the full extent over which significant emission was visible in the published profiles (at the reference frequency) in order to capture the complexity of the magnetar profiles.
References: (1) Morello et al. (2020); (2) Young et al. (1999); (3) Mitra et al. (2020); (4) Camilo et al. (2007c); (5) Camilo et al. (2008); (6) Levin et al. (2010); (7) Levin et al. (2012); (8) Eatough et al. (2013); (9) Camilo et al. (2006); (10) Camilo et al. (2007a); (11) Esposito et al. (2020); (12) Lower et al. (2020).

Object	P (s)	$\dot{P}$ (ss^{-1})	Profile Width (°)	Ref. Freq. (MHz)	References
PSR J0250+5854	23.5	2.72×10^{-14}	2.0	1250	This work
PSR J2144−3933	8.5	4.96×10^{-16}	0.8	1400	2,3
PSR J2251−3711	12.1	1.31×10^{-14}	1.2	1382	1
1E 1547.0−5408	2.1	2.32×10^{-11}	90	6600	4,5
PSR J1622−4950	4.3	1.70×10^{-11}	190	1400	6,7
PSR J1745−2900	3.8	6.80×10^{-12}	15	2400	8
XTE J1810−197	5.5	1.02×10^{-11}	35	1400	9, 10
Swift J1818.0−1607	1.4	9×10^{-11}	20	1548	11, 12

in the published profiles is clearly distinguishable from the noise (rounded to the nearest five degrees).

Looking at Table 2 it is clear there is a stark contrast between the profile widths of the magnetars compared to the slow pulsars, much more than can be expected from just the differences in P (and hence $R_{\rm LC}$). There are four potential geometric explanations for why magnetars have much wider profiles compared to the slow pulsars: 1) all slowly rotating pulsars are observed with an extremely grazing line of sight with respect to the radio beam; 2) for all slowly rotating pulsars only a tiny fraction of the open-field-line region is active; 3) all magnetars have a magnetic axis almost aligned with the rotation axis; 4) magnetars produce radio emission much higher up in the magnetosphere. We will argue that only options 3) and 4) are viable, and that option 4) plays a more significant role. The first option relies on a very unlikely coincidence, and will not be considered further.

It was argued in Sec. 4.2 that only part of the open-field-line region is active for PSR J0250+5854. However, this fraction needs to be very small for this and the other slow pulsars if it is to be the main reason why the slow pulsars have such narrow beams compared to the magnetars. This seems unlikely to be the case, as it would not explain why there are no slow pulsars with multiple narrow profile components spread over a similar fraction of the rotation period for which which magnetars show emission. Instead, the structure of the profiles of the slow pulsars blend together in a single narrow profile, whereas the magnetar profiles have much more complex, multi-component structure. The magnetars often exhibit individual components which are much wider than the full profiles of the slow pulsars.

If magnetars have very aligned radio beams with respect to their rotation axis (small α), the observer's line of sight would spend a larger fraction of the time within the beam – this can be seen by rearranging Eq. (4) for a fixed cone angle ρ and impact parameter β. If true, this suggests that these young objects have beams which become aligned much faster compared to what is believed to happen for normal pulsars (Tauris & Manchester 1998; Weltevrede & Johnston 2008). Polarisation studies of some of the radio magnetars suggest they may have aligned magnetic axes. This was suggested by Camilo et al. (2007b) for XTE 1810−197, although with orthogonal polarisation mode jumps it could be closer to orthogonality as well. Kramer et al. (2007) preferred to interpret the polarisation of this magnetar with a non-aligned, offset dipole or a non-dipolar magnetic field configuration. An aligned magnetic field was suggested for 1E 1547.0−5408 (Camilo et al. 2008), but RVM fitting for PSR J1622−4950 by Levin et al. (2012) suggested a configuration that is not particularly aligned. PSR J2144−3933 is thought to be a nearly orthogonal rotator (Mitra et al. 2020). An issue with attributing small α to magnetars is that it makes it difficult to reconcile with the large modulation of the thermal X-rays, as was highlighted for XTE 1810−197 (Gotthelf & Halpern 2007; Perna & Gotthelf 2008) and 1E 1547.0−5408 (Israel et al. 2010).

Eqs. (3) and (4) can be used to estimate how extreme the alignment of the magnetars should be to explain their wide pulse profiles. Taking the mean magnetar period and median magnetar profile width from Tab. 2 with an emission height of 400 km, such an object requires $\alpha \lesssim 11°$ to produce profiles of the observed width. Overall, the evidence from RVM fitting for magnetars having particularly small α values is mixed and X-ray data seems to preclude very small α. Therefore is is likely that at the very least emission height plays a significant role as well.

Large emission heights for the magnetars imply radio beams (hence pulse profiles) which are wider. If the emission heights are the dominant reason for the magnetars having wider radio profiles, the emission heights need to be ∼20 times larger (around 10,000 km) compared to the slow pulsars. This could potentially be facilitated by the incredible strength of the magnetar magnetic fields. Given the slow rotation of magnetars, this is still only a few per cent of the light cylinder radius, making this a more plausible scenario.

5 CONCLUSIONS

We have obtained the highest- and lowest-frequency radio detections of of the most slowly rotating known pulsar to date, and observed it (PSR J0250+5854) simultaneously at LOFAR frequencies and L-band. The highest frequency detection with FAST (1250 MHz) shows that the spectrum is exceptionally steep with a spectral index of $-3.5^{+0.1}_{-0.5}$ and the lowest frequency detection with NenuFAR reveals a spectral turn-over below 95 MHz. The pulse profile shows a broadening at higher frequencies contrary to the expectations of radius-to-frequency mapping, and this is believed to be due to the emergence of extra profile components, which implies that the beam is underfilled at lower frequencies. The polarisation information of LOFAR data at 150 MHz and FAST data at 1250 MHz was used to constrain the viewing geometry. This shows that the line-of-sight impact parameter β is very small, passing within 2.2°

of the magnetic axis, and confirms that the radio beam is very narrow as expected for such a slow pulsar. Furthermore, the lack of any perceptible A/R effects in the PA swing implies that the emission height of PSR J0250+5854 is low, consistent with the 200 to 400 km range found for other non-recycled pulsars. Finally, we draw comparisons between other slow pulsars, PSR J0250+5854, and the five known magnetars with pulsed radio emission. We note that the profile widths of the magnetars are significantly broader than the normal slow pulsars – we argue that whilst magnetic alignment in magnetars may play a role in explaining this, the main reason is the substantially larger emission heights in magnetars.

ACKNOWLEDGEMENTS

Are there any other institutional/funding things that should go here?

This research has made use of the NASA/IPAC Extragalactic Database (NED) which is operated by the Jet Propulsion Laboratory, California Institute of Technology, under contract with the National Aeronautics and Space Administration. Pulsar research at Jodrell Bank Centre for Astrophysics and Jodrell Bank Observatory is supported by a consolidated grant from the UK Science and Technology Facilities Council (STFC).

REFERENCES

Blaskiewicz M., Cordes J. M., Wasserman I., 1991, ApJ, 370, 643
Bondonneau L., Theureau G., Cognard I., 2018, in SF2A-2018: Proceedings of the Annual meeting of the French Society of Astronomy and Astrophysics. p. Di
Bondonneau L., et al., 2020, A&A, in press.
Camilo F., Ransom S. M., Halpern J. P., Reynolds J., Helfand D. J., Zimmerman N., Sarkissian J., 2006, Nature, 442, 892
Camilo F., Reynolds J., Johnston S., Halpern J. P., Ransom S. M., van Straten W., 2007a, ApJ, 659, L37
Camilo F., et al., 2007b, ApJ, 663, 497
Camilo F., Ransom S. M., Halpern J. P., Reynolds J., 2007c, ApJ, 666, L93
Camilo F., Reynolds J., Johnston S., Halpern J. P., Ransom S. M., 2008, ApJ, 679, 681
Chen K., Ruderman M., 1993, ApJ, 402, 264
Chen J. L., Wang H. G., 2014, ApJS, 215, 11
Chen J.-L., Wang H.-G., Chen W.-H., Zhang H., Liu Y., 2007, Chinese J. Astron. Astrophys., 7, 789
Cordes J. M., 1978, ApJ, 222, 1006
Dai S., et al., 2018, MNRAS, 480, 3584
Desvignes G., Kramer M., Cognard I., Kasian L., van Leeuwen J., Stairs I., Theureau G., 2013, in van Leeuwen J., ed., IAU Symposium Vol. 291, Neutron Stars and Pulsars: Challenges and Opportunities after 80 years. pp 199–202 (arXiv:1211.3937), doi:10.1017/S1743921312023630
Dyks J., Rudak B., 2012, MNRAS, 420, 3403
Dyks J., Rudak B., 2013, MNRAS, 434, 3061
Dyks J., Rudak B., 2015, MNRAS, 446, 2505
Dyks J., Rudak B., Demorest P., 2010, MNRAS, 401, 1781
Eatough R. P., et al., 2013, Nature, 501, 391
Esposito P., et al., 2020, ApJ, 896, L30
Gedalin M., Gruman E., Melrose D. B., 2002, MNRAS, 337, 422
Gil J., Gronkowski P., Rudnicki W., 1984, A&A, 132, 312
Gil J., Lyubarsky Y., Melikidze G. I., 2004, ApJ, 600, 872
Gotthelf E. V., Halpern J. P., 2007, ApJ, 664, L35
Gould D. M., Lyne A. G., 1998, MNRAS, 301, 235
Haberl F., 2007, Ap&SS, 308, 181
Haslam C. G. T., Salter C. J., Stoffel H., Wilson W. E., 1982, A&AS, 47, 1
Hibschman J. A., Arons J., 2001, ApJ, 560, 871
Hotan A. W., van Straten W., Manchester R. N., 2004, Publ. Astron. Soc. Australia, 21, 302
Israel G. L., et al., 2010, MNRAS, 408, 1387
Izvekova V. A., Kuzmin A. D., Malofeev V. M., Shitov I. P., 1981, Ap&SS, 78, 45
Jankowski F., van Straten W., Keane E. F., Bailes M., Barr E. D., Johnston S., Kerr M., 2018, MNRAS, 473, 4436
Jiang P., et al., 2020, Research in Astronomy and Astrophysics, 20, 064
Johnston S., Karastergiou A., 2019, MNRAS, 485, 640
Johnston S., Smith D. A., Karastergiou A., Kramer M., 2020, MNRAS, 497, 1957
Karastergiou A., Johnston S., 2007, MNRAS, 380, 1678
Keith M. J., Johnston S., Weltevrede P., Kramer M., 2010, MNRAS, 402, 745
Keith M. J., Johnston S., Levin L., Bailes M., 2011, MNRAS, 416, 346
Kijak J., Gil J., 2003, A&A, 397, 969
Komesaroff M. M., 1970, Nature, 225, 612
Kramer M., Stappers B. W., Jessner A., Lyne A. G., Jordan C. A., 2007, MNRAS, 377, 107
Lawson K. D., Mayer C. J., Osborne J. L., Parkinson M. L., 1987, MNRAS, 225, 307
Lazarus P., Karuppusamy R., Graikou E., Caballero R. N., Champion D. J., Lee K. J., Verbiest J. P. W., Kramer M., 2016, MNRAS, 458, 868
Levin L., et al., 2010, ApJ, 721, L33
Levin L., et al., 2012, MNRAS, 422, 2489
Lorimer D. R., Kramer M., 2005, Handbook of Pulsar Astronomy. Cambridge University Press
Lower M. E., Shannon R. M., Johnston S., Bailes M., 2020, ApJ, 896, L37
Lyne A., Graham-Smith F., 2012, Pulsar Astronomy, 4 edn. Cambridge University Press
Majid W. A., Pearlman A. B., Dobreva T., Horiuchi S., Kocz J., Lippuner J., Prince T. A., 2017, ApJ, 834, L2
Malofeev V. M., Malov I. F., 1980, Soviet Ast., 24, 54
Manchester R. N., et al., 2010, ApJ, 710, 1694
Michel F. C., 1987, ApJ, 322, 822
Mitra D., Rankin J. M., 2002, ApJ, 577, 322
Mitra D., Basu R., Melikidze G. I., Arjunwadkar M., 2020, MNRAS, 492, 2468
Morello V., et al., 2020, MNRAS, 493, 1165
Nan R., et al., 2011, International Journal of Modern Physics D, 20, 989
Olausen S. A., Kaspi V. M., 2014, ApJS, 212, 6
Perna R., Gotthelf E. V., 2008, ApJ, 681, 522
Pilia M., et al., 2016, A&A, 586, A92
Radhakrishnan V., Cooke D. J., 1969, Astrophys. Lett., 3, 225
Radhakrishnan V., Rankin J. M., 1990, ApJ, 352, 258
Rankin J. M., 1983a, ApJ, 274, 333
Rankin J. M., 1983b, ApJ, 274, 359
Rankin J. M., 1990, ApJ, 352, 247
Rankin J. M., 1993, ApJ, 405, 285
Reich P., Reich W., 1988, A&A, 196, 211
Rookyard S. C., Weltevrede P., Johnston S., 2015, MNRAS, 446, 3367
Ruderman M. A., Sutherland P. G., 1975, ApJ, 196, 51
Sanidas S., et al., 2019, A&A, 626, A104
Shimwell T. W., et al., 2017, A&A, 598, A104
Sieber W., 1973, A&A, 28, 237
Slee O. B., Dulk G. A., Otrupcek R. E., 1980, Proceedings of the Astronomical Society of Australia, 4, 100
Stappers B. W., et al., 2011, A&A, 530, A80
Sturrock P. A., 1971, ApJ, 164, 529
Tan C. M., et al., 2018, ApJ, 866, 54
Tauris T. M., Manchester R. N., 1998, MNRAS, 298, 625
Thorsett S. E., 1991, ApJ, 377, 263
Timokhin A. N., 2010, MNRAS, 408, 2092
Véron-Cetty M. P., Véron P., 2006, A&A, 455, 773
Wang H. G., et al., 2014, ApJ, 789, 73
Wardle J. F. C., Kronberg P. P., 1974, ApJ, 194, 249
Weltevrede P., 2016, A&A, 590, A109
Weltevrede P., Johnston S., 2008, MNRAS, 387, 1755

Young M. D., Manchester R. N., Johnston S., 1999, Nature, 400, 848
Zhang B., Harding A. K., Muslimov A. G., 2000, ApJ, 531, L135
van Heerden E., Karastergiou A., Roberts S. J., 2017, MNRAS, 467, 1661
van Kerkwijk M. H., Kaplan D. L., 2007, Ap&SS, 308, 191
van Leeuwen J., Stappers B. W., 2010, A&A, 509, A7
van Straten W., Bailes M., 2011, Publ. Astron. Soc. Australia, 28, 1

This paper has been typeset from a TEX/LATEX file prepared by the author.